# Nanoscale

Accepted Manuscript


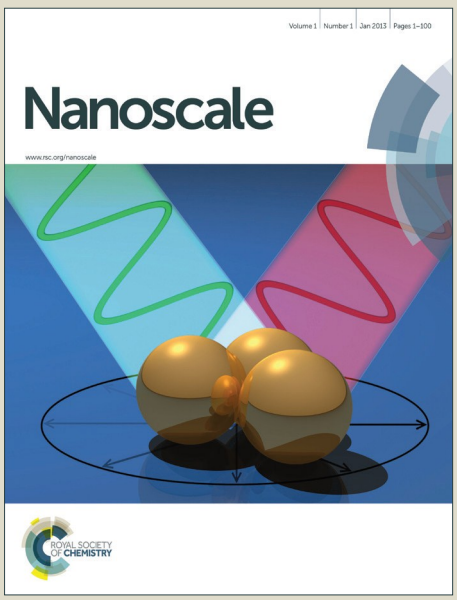





ROYAL SOCIETY OF CHEMISTRY

www.rsc.org/nanoscale

Nanoscale

ARTICLE

# PRED treatment mediated stable and efficient water oxidation performance of $Fe_2O_3$ nano-coral structure†

Received 00th January 20xx,
Accepted 00th January 20xx

DOI: 10.1039/x0xx00000x

www.rsc.org/

Pravin S. Shinde, [a] Hyun Hwi Lee, [b] Su Yong Lee, *[b] Young Mi Lee, [b] and Jum Suk Jang*[a]

Herein, we demonstrate that an electrochemical surface treatment of Fe foil with simple pulse reverse electrodeposition (PRED) prior to thermal oxidation can substantially enhance the photoelectrochemical (PEC) stability and water splitting performance of $Fe_2O_3$/Fe photoanodes. Comprehensive structural (XRD, FESEM, HRTEM), compositional (XPS depth profiling), and electrochemical (EIS, Mott-Schottky) analyses were performed to understand the effect of PRED treatment on PEC performance of fabricated photoanodes. It is revealed that air-exposed Fe foil is prone to formation of a loosely bound surface oxide layer that, upon annealing at 800 °C, results in an unstable $Fe_2O_3$ nano-flake (2-3 μm long) morphology. In contrast, when such Fe foil is pre-treated with PRED to etch the loosely bound oxide layer, adherent inverse-opal-like nano-coral structures (60-100 nm thin) are formed. In addition to stability improvemnet, PRED-treatment also assists in exposing the photocatalytically active high index [104] facet sites of hematite. Thin hematite nano-coral structures with high index [104] facet sites significantly improved the separation of photo-generated charge carriers and oxygen evolution kinetics, resulting in performance enhancement with excellent photocurrent stability for extended duration in a 1M NaOH solution under one sun illumination. The net photocurrent density for nano-coral morphology was 0.813 mA $cm^{-2}$ at 1.23 V vs. RHE, which is the highest reported value for pristine hematite photoanodes fabricated from Fe foil.

## Introduction

An earth-abundant and non-toxic hematite ($\alpha$-$Fe_2O_3$) photoanode material has been the choice for water oxidation reactions, because of its narrow band gap (~2.1 eV) with a maximum theoretical STH conversion efficiency (15%).[1] However, hematite photoanodes suffer from high photoactivity loss due to poor electrical conductivity, low absorption coefficient,[2] deep visible light penetration ($\alpha^{-1}$ =118 nm at $\lambda$ = 550 nm),[3] short hole-diffusion length (2−4 nm),[4] and short excited-state lifetime (<10 ps). Hence, researchers have focused on the fabrication of nano-architectures that increase the chances of photo-generated holes reaching the oxide/electrolyte interface, while allowing efficient light absorption.[5-7] Nano-architectures with a high aspect ratio that particularly allow incident photons to be absorbed close to the electrode–electrolyte interface are beneficial.[8] Recently, thermal oxidation of iron foil has received intensive interest due to its technical simplicity and large-scale growth capabilities in fabrication of $\alpha$-$Fe_2O_3$ photoanodes with three-dimensional nano-architectures, most often with high aspect-ratio structures such as nanorods, nanoflakes/nanobelts, nanowires, or nanograss.[9-15] Moreover, growing hematite on iron foil is advantageous as it enables efficient transport of photo-generated majority charge carriers (electrons) through the hematite layer to the back contact of the photoanode, thereby mediating the poor conductivity problem observed in hematite. Several studies on thermally oxidized $\alpha$-$Fe_2O_3$ nanostructures revealed that the process parameters such as annealing temperature and annealing environment affect the morphology, aspect ratio, and oxide thickness in a relatively predictable way. For instance, oxidation of Fe foil at 800 °C in air leads to the formation of nanobelts (diameter ~50−100 nm). At 450 °C, similar treatment results in the formation of high aspect-ratio nanoflakes.[16] Annealing in air at 550−650 °C for longer duration results in nanowires.[10] Nanorods were obtained by annealing Fe foil in an oxygen-rich atmosphere, whereas annealing in oxygen-lean atmosphere yields a nanocoral-like morphology.[14] Synthesis of thermally oxidized iron oxide nanostructures typically involves low-temperature annealing in the range of 300−700 °C for several hours,[10, 15] with or without different gas environments.[17] Despite fascinating nanostructured morphologies, only few studies on the photoelectrochemical (PEC) performance of thermally oxidized $Fe_2O_3$/Fe photoanodes have been performed,[11, 14, 18] distinctly due to poor photocurrent response on the order of 0.3−0.5 μA $cm^{-2}$ at 1.23 V vs. RHE and very high dark currents.[14] This infers that the grown nanostructures have weak attachment to the Fe foil and are unstable in

[a] Division of Biotechnology, Advanced Institute of Environmental and Bioscience, College of Environmental and Bioresource Sciences, Chonbuk National University, Iksan 570−752, Republic of Korea. E-mail: jangjs75@jbnu.ac.kr
[b] Pohang Accelerator Laboratory (PAL), Pohang University of Science and Technology (POSTECH), Pohang 790−784, Republic of Korea. E-mail: dsleesy@postech.ac.kr

† Electronic Supplementary Information (ESI) available: [*J*–*V* curves, Rietveld analysis from Synchrotron-irradiated XRD, In-house XRD, FESEM, HR-TEM, XPS, and UV−vis spectroscopy]. See DOI: 10.1039/x0xx00000x

electrolytes. The existence of high dark current was attributed to exposure of the underlying metallic Fe/$Fe_3O_4$ substrate to the electrolyte.[16] The high dark current affects the chemical stability, eventually limiting the net photocurrent density and device performance. In the worst case, it can result in permanent damage of the photoanodes. The dark current issues can be addressed through surface chemical treatments of iron foil using HF or HCl, but such treatments occasionally damage the photoanodes. In such a scenario, a simple and inexpensive pulse reverse electrodeposition (PRED) method, which is based on adsorption-desorption phenomena at the electrode-electrolyte interface, using a weak electrolyte is an easy alternative. Herein, we investigate the nanoscale-level developments of Fe foil due to the electrochemical surface treatment with PRED before thermal oxidation at 800 °C that eventually affect its surface properties to improve the photoelectrochemical (PEC) stability and water splitting performance of the $Fe_2O_3$/Fe photoanodes.

## Experimental

### Materials and fabrication of iron oxide photoanodes

A high-purity iron sheet (0.1 mm, 99.99% purity, Alfa Aesar) was cut into foils (2 cm× 0.6 cm × 0.01 cm), polished with fine-grade SiC paper, cleaned ultrasonically in acetone and ethanol (for 5 min each), rinsed with deionized water, and finally dried under $N_2$ prior to use. The chemicals were purchased from Alfa Aesar, Kanto, and Junsei Chemicals and were used without further purification. The solutions were prepared using high-purity deionized water (Scholar type, Human Power I$^+$ Corp., resistivity < 18 MΩ cm).

Iron oxide photoanodes were prepared via thermal oxidation of polished Fe foils at high temperature (800 °C) for a short time. Two different kinds of Fe foils were used—one with electrochemical treatment of PRED and one without (bare Fe foil). The PRED treatment was performed in a two-electrode cell using a weak electrolyte consisting of 0.15 g ascorbic acid, 0.05 g amidosulfonic acid, and 1.5 g boric acid in 0.1 L deionized water. The process parameters of PRED, such as amplitude of square wave pulse (10V [–6 / +4 V]), duty cycle (20%), pulse period (10 ms), and deposition time (300 s), were kept constant.[19] After PRED treatment, the samples were rinsed in deionized water and dried under $N_2$. Finally, bare and PRED-treated samples were annealed using a one-step method that involves quenching of samples in air after soaking them in a box furnace at 800 °C for a short duration and then subsequent transfer to an oven at 100 °C for 10 min.[20] The annealing and PRED-treatment times were optimized systematically by assessing the photocurrent responses of the photoanodes. The annealing time was varied from 4 to 15 min. Later, the pulse time hereafter termed as 'PRED time' was also varied from 2 to 25 min. The surfaces of the annealed samples appeared greyish in contrast to the bare sample, which was dark reddish in color. The iron oxide coatings of the PRED-treated samples exhibited excellent adhesion to the Fe foil, while those prepared using bare Fe foil showed poor scotch-tape adhesion test. For comparison, the iron oxide electrodes were also fabricated at low temperature (600°C up to 4 h) by conventional annealing approach (heating at 5°C min$^{-1}$ and cooling naturally).

### Characterization

The concentration of iron species that dissolute in electrolyte during the PRED treatment of Fe foil was determined using an inductively coupled plasma-atomic emission spectrometer (ICP-AES, Leeman Labs, USA). The preliminary structural analysis of the photoanodes was performed using in-house X-ray diffraction (XRD) patterns, which were recorded on a PANalytical X'pert Pro MPD diffractometer equipped with a Cu–Kα radiation source ($\lambda_{K\alpha 1}$=1.540598 Å) operated at 40 kV and 30 mA. XRD patterns were recorded in the range of 20−70° with a step size of 0.0167 ° s$^{-1}$. The preferential ordering and contributed amount of iron oxide phases on the iron oxide/iron photoanodes were obtained via measurement of two-dimensional X-ray diffraction (2D-XRD) patterns by probing at an X-ray wavelength of 0.1072 nm (11.57 keV). The sample-to-detector distance (SDD) during the measurement of diffraction profiles using a two-dimensional (2D) image plate detector was 256 mm. In order to emphasis and analyse the near-surface region of the photoanodes, the X-ray incident angle was selected as 3°, at which the X-ray attenuation length was ~1.2 μm; otherwise a conventional θ-2θ scan continuously changes the attenuation length with increasing incident angle of 'θ'. The 2D-XRD measurements were performed at the 5A X-ray scattering (5A XRS) beamline for materials science at the Pohang Light Source II (PLS-II) in Korea. The growth morphology and chemical composition of the oxidized samples were examined using a field emission scanning electron microscope (FESEM, SUPRA 40VP, Carl Zeiss, Germany) equipped with an X-ray energy dispersive spectrometer (EDX). The surface composition and chemical species of the bare, PRED-treated, and annealed iron (oxide) samples were studied using X-ray photoelectron spectroscopy (XPS) combined with $Ar^+$ sputter depth profiling. The surface of each sample was initially cleaned with $Ar^+$ ion (high purity 99.999%) sputtering at a beam energy of 2 kV under a chamber base pressure of $1.0\times10^{-6}$ Torr. The XPS spectra were obtained using synchrotron radiation at the 10D HRXPS beamline of Pohang Accelerator Laboratory (PAL). A photon energy of 830 (837.44) eV was used to obtain high-quality XPS spectra. The photoelectron signals were recorded with a PHOIBOS 150 electron energy analyzer equipped with a two-dimensional charge-coupled device (2D CCD) detector (Specs GmbH), collecting the photoelectrons from the surface normal. The binding energy (BE) scale was calibrated with an Au 4f core-level peak at 84.0 eV.[21] The base pressure of the main chamber was maintained $1.2\times10^{-10}$ Torr. A survey spectrum was first recorded to identify all elements present at the surface, and then high-resolution spectra of the Fe 2p and O 1s regions were recorded. Depth profiling is a useful tool for investigating the surface layer of photoanodes that are influenced by different kinds of chemical environments. Depth profiling was performed by altering the sputtering times to 0, 10, 30, 60, and 120 s. The processing of XPS data involving peak de-

convolutions with Shirley background was achieved using XPS Peak-fit program. The experimental data were analysed without preliminary smoothing. High-resolution transmission electron microscopy (TEM Tecnai G2 T20 U-Twin) images were recorded for bare and PRED-treated samples annealed at identical conditions. The TEM samples were prepared by dispersing the sample ultrasonically in ethanol for 5 min and placing the few drops of resulting suspension onto the copper grid and drying in air. The optical properties of representative $Fe_2O_3$/Fe photoanodes were studied using an UV-vis-NIR spectrophotometer (Shimadzu, UV-2600 series) with an integrating sphere attachment, using $BaSO_4$ as a reference. The diffuse reflectance spectra were collected in the wavelength range of 350−800 nm. The diffuse reflectance spectra of the samples were transformed by Kubelka−Munk function, $F(R_\infty)$ using a relation:[22]

$$F(R_\infty) = (1-R)^2/2R \quad (1)$$

where R is the diffuse reflectance of the sample.

**Photoelectrochemical measurement**

The PEC measurements of the $Fe_2O_3$/Fe photoanodes were carried out in a PEC cell consisting of a three-arm glass compartment with a circular quartz window for light illumination. The PEC cell was comprised of $Fe_2O_3$/Fe as the working electrode, Pt wire as the counter electrode, Ag/AgCl (saturated with KCl) as the reference electrode, and 1 M NaOH as the electrolyte. All potentials were measured relative to that of the Ag/AgCl electrode (sat. KCl) and were revised for the reversible hydrogen electrode (RHE) scale using the Nernst equation.[8] One sun light illumination (100 mW $cm^{-2}$, AM1.5) was provided using a solar simulator (Abet Technologies). Photocurrent density−voltage (*J*–*V*), electrochemical impedance spectroscopy (EIS), and Mott−Schottky (MS) studies were performed using a potentiostat (Ivium, Netherland) equipped with an electrochemical interface and impedance analyzer facility. To verify the reproducibility of PEC performance, three sets of similar $Fe_2O_3$/Fe photoanodes were prepared on different days under identical conditions for each parameter. The EIS study was performed under one sun illumination at 1.23 $V_{RHE}$. The MS study was performed under dark conditions with a DC applied potential window of −0.6 to 0.4 V vs. Ag/AgCl at the AC frequency of 0.5 kHz. The amplitude of the AC potential was 10 mV for both EIS and MS measurements. The EIS data were validated fitted to the equivalent circuit model using the ZView program based on the nonlinear least-squares Levenberg-Marquardt algorithm.

## Results and Discussion

The iron oxide electrodes fabricated at low temperature 600°C up to 4 h by conventional annealing (heating at 5°C $min^{-1}$ and cooling naturally) of PRED-treated Fe foil exhibited a net photocurrent density ($J_{ph}$, difference between light and dark currents) of ~650 μA $cm^{-2}$ at 1.23 V vs. RHE ($V_{RHE}$) with huge contribution of dark currents (Fig. S1). However, encouraging results were obtained by following a rapid high-temperature (800 °C) annealing approach.[20] Fig. 1a shows the variation in $J_{ph}$ at 1.23 $V_{RHE}$ obtained from *J*–*V* curves (Fig. S2a) of 5 min PRED-treated $Fe_2O_3$/Fe photoanodes prepared at 800 °C for different annealing times and a bare $Fe_2O_3$/Fe photoanode annealed at 800 °C for 6 min. Among all photoanodes tested, the PRED-treated $Fe_2O_3$/Fe annealed at 6 min demonstrated a net $J_{ph}$ of 813 μA $cm^{-2}$ at 1.23 $V_{RHE}$. This is the highest ever reported photocurrent for a thermally oxidized pristine hematite photoanode synthesized using Fe foil in a box furnace under ambient conditions (without any controlled oxygen-rich environment).[11, 14, 18, 23] Though it is not the highest photocurrent reported for hematite fabricated on FTO-coated glass substrates where intentional or unintentional Sn doping plays crucial role in improving the photocurrent dramatically.[24] The results in present study are promising since the photocurrent of PRED-treated pristine $Fe_2O_3$/Fe photoanodes could further be improved upon doping. Moreover, metal based photoanodes are advantages for accelerating their use in scale-up deployment.

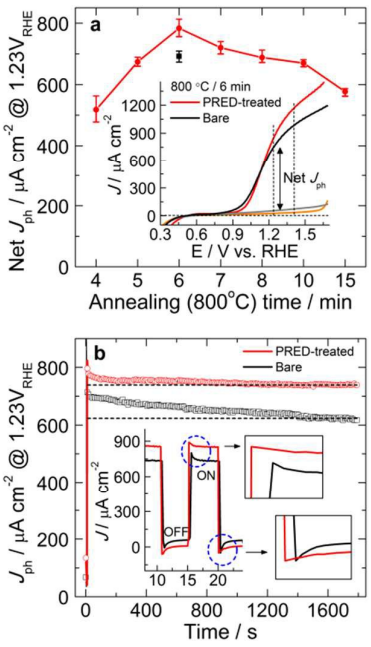


**Fig. 1** (a) $J_{ph}$ variation at 1.23 $V_{RHE}$ for PRED-treated $Fe_2O_3$/Fe photoanodes prepared at 800 °C with different annealing times. The error bars represent the standard deviations in *J*–*V* measurements. Inset of Fig. 1a shows the *J*–*V* curves of bare and PRED-treated $Fe_2O_3$/Fe photoanodes annealed at 800 °C for 6 min, and Fig. 1b shows the corresponding photo-stability curves. Magnified portions show the current-responses under chopped illumination (100 mW $cm^{-2}$) at 1.23 $V_{RHE}$ in 1 M NaOH.

On the contrary, the photocurrent for the $Fe_2O_3$/Fe photoanode prepared under identical conditions but without electrochemical treatment by PRED exhibited a lower photocurrent with major contribution of dark currents on the order of 57 μA $cm^{-2}$ at 1.23 $V_{RHE}$, which eventually decreased the net photocurrent density to 696 μA $cm^{-2}$ at 1.23 $V_{RHE}$. The $J_{ph}$ difference was obviously higher at 1.4 $V_{RHE}$. There was no obvious change in the photocurrent onset potential ($V_{onset}$), with values of 0.96 and 1.0 $V_{RHE}$ for bare and PRED-treated photoanodes, respectively. Bare $Fe_2O_3$/Fe photoanodes demonstrated a poor scotch-tape

adhesion test. Hence, to further analyse the photoelectrochemical stability, chronoamperometry tests of the photoanodes were carried out at 1.23 $V_{RHE}$ for 30 min under one sun illumination (Fig. 1b). The photocurrent of the PRED-treated photoanode was stable for a significantly longer time with only a 3% decrease after continuous illumination. In contrast, the $J_{ph}$ percentage decrease of the bare photoanode was almost 11% for a similar extended time. This suggests that PRED-treatment helps in improving the surface properties of Fe foil before thermal oxidation. Recently, Schäfer *et al.* demonstrated that the oxygen evolution electrocatalytic performance as well as chemical stability of iron oxide can be improved to a great extent via surface oxide modification on stainless steel.[25, 26] The inset of Fig. 1b shows the current response under chopped light illumination for both photoanodes and shading light on the dynamics of photo-generated charge carriers. The photo-response was faster for the PRED-treated $Fe_2O_3$/Fe photoanode, as demonstrated by the sharp rise and decay of current during chopping. The PRED-treatment time was also varied, but the 5 min duration was found to be the optimum (Fig. S2b).

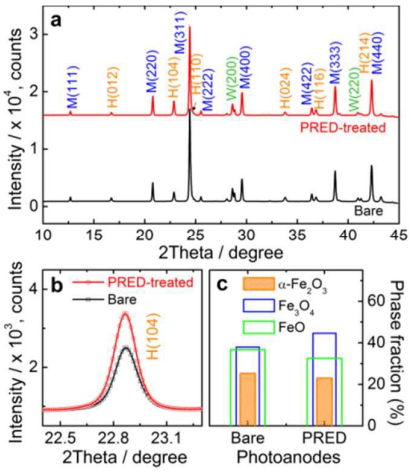


**Fig. 2** (a) Synchrotron XRD (λ=0.107 nm) profiles and (b) G-L fits of the hematite (104) peak for corresponding bare (black) and 5 min PRED-treated (red) photoanodes annealed at 800 °C. The letters 'H', 'M', and 'W' represent the hematite ($Fe_2O_3$), magnetite ($Fe_3O_4$), and wustite (FeO) phases, respectively. (c) Phase quantification was obtained from XRD profiles via Rietveld analysis.

Fig. 2a shows the XRD profiles of bare and PRED-treated iron oxide photoanodes annealed at 800 °C for 6 min. From the diffraction profiles, three dominant phases of iron oxide, photoactive hematite (α-$Fe_2O_3$, denoted as H), magnetite ($Fe_3O_4$, denoted as M), and wustite (FeO denoted as W), were observed with different contribution values. It is common to have non-photoactive phases like $Fe_3O_4$ and FeO in thermally oxidized metal foil-based photoanodes. Phase quantification was performed by fitting the XRD profiles using Rietveld method and a GSAS software package.[27] The analysis revealed similar hematite contributions with phase fractions of 25% and 23% for bare and PRED-treated photoanodes, respectively. Fig. 2c depicts the obtained fractions of H, M, and W phases from Rietveld analysis (Fig. S3). The intensity of the (104) hematite peak for PRED-treated sample was higher than that for other samples (Fig. 2b, Figs. S4-S5). This clearly suggests that PRED treatment preferably helps expose the photo-catalytically-active high index [104] facets. The surface $Fe^{3+}$ plays a key role in heterogeneous photo-catalytic reaction via the redox cycle between $Fe^{3+}$ and $Fe^{2+}$ to generate hydroxyl radicals (•OH). It has been reported that the density of exposed $Fe^{3+}$ on [104] planes of hematite is higher than that of [012] planes, indicating that [104] planes are more reactive than [012] planes and provide more catalytically-active sites to facilitate water oxidation reaction.[28] To further clarify the preferential ordering effect on the phase fraction quantification via diffraction intensity, 2D XRD patterns were measured (Figs. 3a and 3b).

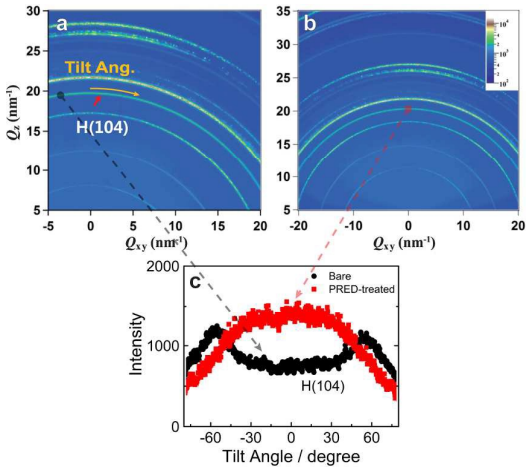


**Fig. 3** (a-b) Synchrotron radiated 2D XRD patterns of (a) bare and (b) 5 min PRED-treated $Fe_2O_3$/Fe photoanodes annealed at 800 °C for 6 min. (c) Hematite (104) circular line cut profiles of bare and PRED-treated photoanodes. The zero degree tilt angle corresponds to the surface normal direction.

Fig. 3c shows the circular line cuts passing through the hematite (104) peak. The maximum intensity of the PRED-treated sample (red squares) at 0° represents the preferential ordering of hematite (104), while the different intensity distribution of the bare sample (black circles) implies that the preferential direction was tilted to ~60° from the normal surface. These diffraction patterns clearly demonstrate that the PRED-treated photoanode had a moderately aligned hematite (104) surface. Therefore, the apparent higher intensity of the hematite (104) peak, as shown in Fig. 2b, does not directly yield a greater hematite phase when considering the preferential ordering. This preferential ordering was considered during diffraction profile analysis.

Figs. S6a–b show the surface morphologies of bare and PRED-treated Fe foils before annealing. Small interconnected grains were seen due to PRED treatment, unlike the plain surface for bare Fe foil. Upon annealing at 800 °C for 6 min, two different morphologies of iron oxide were observed (Figs. 4a-b). A bare annealed $Fe_2O_3$/Fe photoanode showed the typical nano-flake (NF) morphology growing from a thin hematite layer (60–100 nm). NFs were 3–4 μm long and 20–30 nm thick. On the contrary, the PRED-treated $Fe_2O_3$/Fe photoanode revealed inverse-opal-like nano-coral structures

(without NFs) with voids of about 200−300 nm. In connection with phase fraction analysis from Fig. 2c, it is quite clear that the hematite contribution in the bare annealed photoanode comes from a thin hematite layer and NFs (H1+H2), as shown in Fig. 4c. On the other hand, the hematite contribution in the PRED-treated sample comes alone from the thin nano-coral structures (H1), as shown in Fig. 4d. Nano-coral thickness varied from 60−100 nm. Nano-coral morphology not only increased the surface area, but also shortened the distance that holes need to travel to reach the photoanode surface. This is an effective way to increase electron−hole separation before they are recombined on the surface or at the electrolyte interface. Figs. S6−S9 show the surface and cross-sectional FESEM images of $Fe_2O_3$/Fe photoanodes prepared at different annealing and PRED times. The nano-coral voids expanded in size with an increase in annealing time. However, no significant changes were observed with different PRED-treatment times.

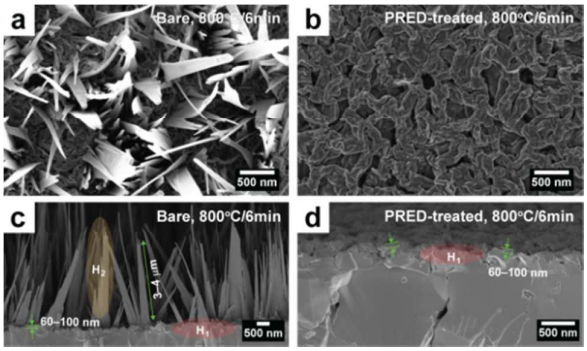


**Fig. 4** (a-b) Surface and (c-d) cross-sectional FESEM images of bare and PRED-treated Fe foil annealed at 800 °C for 6 min, revealing nano-flake and nano-coral structures.

Fig. S10 shows the low-magnification TEM image of single NF with a tip diameter ranging from 20−40 nm and length of 3−4 μm grown perpendicular through the α-$Fe_2O_3$ surface. The NF has a shaped tip and a relatively wide base with high aspect ratio geometry. The HRTEM images and FFT patterns reveal that the NF and nano-coral morphologies were crystalline with rhombohedral crystal structure, in agreement with the XRD study. Their lattice spacing of 0.269 or 0.268 nm correspond to the *d*-spacing of [104] plane. Fig. S11 shows the XPS survey spectra recorded during depth profiling of bare and 5 min PRED-treated Fe foil before and after one-step annealing at 800 °C for 6 min. The photoelectron peaks observed at binding energies (BEs) of 711, 530, 486, 93, and 55 eV were assigned to Fe2p, O1s, C1s, Fe3s, and Fe3p photo-electrons, respectively.The broad peaks centered at 974 eV and 897, 848, and 785 eV were assigned to the $O_{KLL}$, $Fe_{LML}$, and Auger transitions, respectively. Fig. 5 shows the high resolution XPS spectra of the Fe2p and O1s regions for bare and 5 min PRED-treated Fe foil samples. In the O1s region (Figs. 5a-b) of as-received samples, the lowest BE peak centered at 529.5±0.2 eV for bare and PRED-treated samples was assigned to oxygen atoms in the $Fe_2O_3$ phase of iron oxide lattice ($O^{2-}$), O1s (Fe−O). A broad peak next to the higher-energy peak located at 531.2±0.2 eV for both samples was assigned to adsorbed OH ($OH_{(ads)}$) species, carbonate species, or water molecules on the oxide surfaces. The contribution of $OH_{(ads)}$ species was relatively higher in the PRED-treated sample.

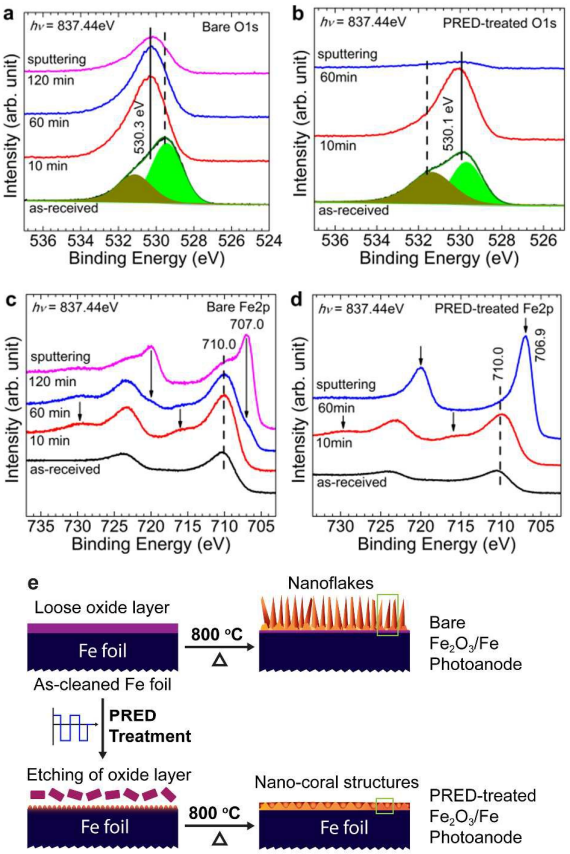


**Fig. 5** High-resolution XPS spectra of (a-b) O1s and (c-d) Fe2p for bare and PRED-treated Fe foil during depth profile analysis. Sputtering time was 10, 60, and 120 min. (e) Schematic showing the formation of nano-flake and nano-coral morphologies.

In the Fe2p region (Figs. 5c-d), the $Fe2p_{3/2}$ and $Fe2p_{1/2}$ peaks of the unannealed samples were located at 710.3±0.2 and 724.0±0.2 eV, respectively. This shows that the as-cleaned Fe foil was partially oxidized. However, the lower intensity of Fe2p peaks in the case of PRED-treated sample suggests etching of the oxide layer due to PRED-treatment. During $Ar^+$ sputtering depth of 10 min, the chemical states of O and Fe were changed. The O1s (Fe−O) peak was shifted toward higher BE, indicating the formation iron oxide ($Fe_3O_4$) with a $Fe^{2+}$ oxidation state. Moreover, the adsorbed OH species were minimal. The nature of Fe2p spectra in both the samples was typical for the $Fe_3O_4$ phase of iron oxide. After 60 min of sputtering, the oxide layer still existed in the bare sample. However, the appearance of a diminishing O1s peak in the PRED-treated sample indicated that the oxide layer no longer existed at sputtering times longer than 60 min. This was also well reflected in the Fe2p spectrum, wherein the occurrence of a sharp peak at 706.9 eV was an indication of zero-valent metallic Fe. However, the bare sample still showed an oxygen peak in the O1s spectrum and a small metallic Fe peak, meaning that $Fe_3O_4$ and FeO phases coexisted. These two phases were present even at a sputtering time of 120 min.

Hence, it can be concluded that PRED-treatment removes the unwanted loosely bound $Fe_3O_4$ oxide layer from the top surface. Fig. S12 shows high-resolution spectra of the Fe2p, and O1s regions for bare and PRED-treated samples annealed at 800 °C for 6 min. The top surface in both samples was $Fe_2O_3$ with a $Fe^{3+}$ oxidation state. After a sputtering time of 10 min, the $Fe^{3+}$ oxidation state in the bare annealed sample changed to $Fe^{2+}$, suggesting the existence of a $Fe_3O_4$ phase. However, the $Fe^{3+}$ oxidation state was retained in the PRED-treated annealed sample. At a sputtering time of 60 min, both tsamples exhibited an $Fe^{2+}$ oxidation state forming $Fe_2O_3$ phase. No obvious metallic peak was observed. The above results suggest that the PRED-treated annealed sample was hematite-rich at least up to the sputtering time of 10 min, which is in good agreement with XRD observations. Fig. 5e shows the schematic illustration of formation of NF and nano-coral morphologies under different growth conditions. As seen from XPS results, as-cleaned bare Fe foil was prone to oxide layer formation in ambient air, which upon annealing produces the NFs originating from the oxide layer. The iron oxide photoanodes prepared without PRED-treatment exhibited poor scotch-tape adherence, meaning that the NFs were not stable. In the present study, PRED treatment with an acidic electrolyte (without any cationic or anionic species to be reduced) involved the application of cathodic and anodic pulses switched at −6 V and +4 V over a short duration. Without any reducible species in the electrolyte, the surface of the metal foil was etched by selectively dissolving the loose surface-bound $Fe_2O_3$ oxide layer from the iron foil. This is in agreement with the FESEM study, wherein a noticeable change in surface morphology of the Fe foil was observed after PRED treatment in comparison with that of bare Fe foil. This shows that the effect of surface treatment with PRED is to effectively modify the oxide nucleation locations that define the growth shapes. Such treatment eventually activates the surface of Fe foil for thermal oxidation, resulting in stable nano-coral morphology. To further confirm the oxide layer dissociation by the action of PRED, ICP-AES analysis of the acidic electrolyte before and after PRED treatment was carried out. No iron content was detected in unused fresh electrolyte. However, iron content (60.18 μg $L^{-1}$) was detected from the electrolyte solution after a 5 min PRED treatment. The nature of the surface dictates the nanostructure growth. Recently, it was demonstrated that a fine or flat Fe foil surface resulted in nanowire formation, while a high surface roughness of Fe foil resulted in dominant formation of nano-blades.[15] The growth mechanism of $Fe_2O_3$ nanoflakes via thermal oxidation has been previously studied.[13] Growth of nano-structures at high annealing temperatures might be dominated by a vapour−solid (VS) mechanism. Fig. S13 shows the Kubelka−Munk plot of bare and PRED-treated iron oxide photoanodes annealed at 800 °C for different annealing times and different PRED times. The indirect band gap energy ($E_g$) estimated for all the samples was in the range of 2.11−2.23 eV, which corresponds to the typical $E_g$ values of hematite.

The electron transfer processes occurring across the electrolyte and the surface of the photoanode were investigated using electrochemical impedance spectroscopy (EIS). Fig. 6a shows the Nyquist plots (real vs. imaginary impedance) of bare and PRED-treated $Fe_2O_3$/Fe photoanodes prepared at 800 °C for 6 min at a bias potential of 1.23 $V_{RHE}$ under one sun illumination. The EIS results were fitted using circuit elements consisting of one resistor and two parallel RC circuits.[29] A constant phase shift element (CPE) meant for imperfect capacitance was often used. Only one semicircle is seen in the Nyquist plot, the diameter of which denotes the charge-transfer resistance. Table 1 shows the results of EIS fitting. The series resistance ($R_s$) and charge transfer resistance ($R_{ct,trap}$) were lower for the PRED-treated $Fe_2O_3$ photoanode in comparison with that of bare $Fe_2O_3$ photoanode. The reduced $R_{ct}$ indicates that the charge transfer at the PRED-treated photoanode/electrolyte interface was significantly improved. The values of charge carrier concentration or the donor density ($N_D$) of the representative α-$Fe_2O_3$ photoanodes were estimated from the Mott−Schottky analysis.[7]

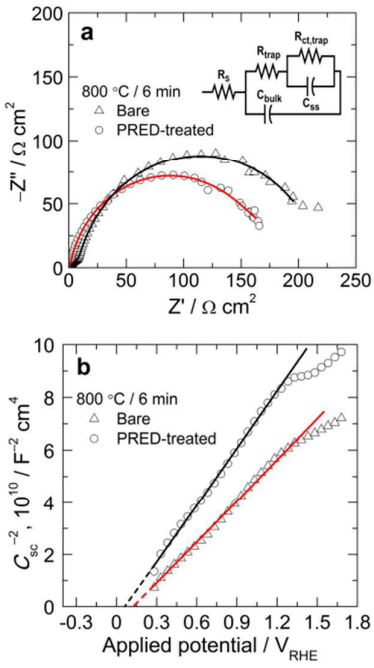


**Fig. 6** (a) Nyquist plots of bare and PRED-treated $Fe_2O_3$/Fe photoanodes prepared with 5 min PRED-treatment by one-step annealing at 800 °C for 6 min. Electrolyte was 1 M NaOH, and the light was one sun illumination. The inset of Fig. 5a shows the equivalent electrochemical circuit. Discrete symbols and the solid lines/curves represent the experimental data and the results of fitting, respectively.

**Table 1**. Parameters from EIS study of bare and PRED-treated $Fe_2O_3$/Fe photoanodes.

| $R$ / Ω cm² | $R_s$ | $R_{trap}$ | $R_{ct,trap}$ |
|---|---|---|---|
| $C_{[CPE]}$ / μF | | $C_{bulk}$ | $C_{ss}$ |
| Bare photoanode | 9.83 | 79.50 | 1501 |
| | | 2.95 | 10.61 |
| PRED-treated photoanode | 5.62 | 1364 | 457 |
| | | 9.30 | 697 |

Fig. 6b shows the Mott–Schottky plot (inverse-square of space charge capacitance ($C_s$) versus applied potential) for bare and

PRED-treated $Fe_2O_3$/Fe photoanodes. The positive slope confirmed the n-type semiconducting behaviour of $Fe_2O_3$/Fe photoanodes. From the slope of the Mott–Schottky plots, the $N_D$ values for bare and PRED-treated $Fe_2O_3$/Fe photoanode were determined to be $3.36 \times 10^{19}$ and $2.43 \times 10^{19}$ $cm^{-3}$, respectively. The corresponding flat band potential ($V_{fb}$) values were 0.129 and 0.067 $V_{RHE}$, respectively. The $N_D$ values were similar for the bare and PRED-treated photoanodes, although the slightly higher $N_D$ value for the bare photoanode was ascribed to a higher contribution from the FeO phase, which is supposedly more conducting than $Fe_3O_4$.[30]

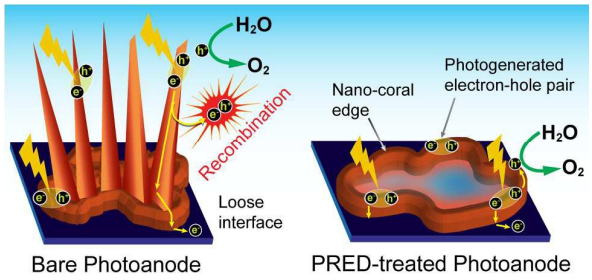


**Fig. 7** Schematic showing the charge transfer mechanism in bare and PRED-treated $Fe_2O_3$/Fe photoanodes prepared at 800 °C for 6 min.

Fig. 7 shows the schematic of charge transfer in bare and PRED-treated photoanodes. Since hematite has short hole-diffusion length and excited-state lifetime, the distance between its nano-architecture and the back contact has to be minimal so that the photogenerated electron and holes could be separated effectively and then transferred to the back contact and electrolyte, respectively. The bare photoanode with nano-architectures consisting of about 3−4 μm long NFs with longer pathways and a loose interface adjoining the base was detrimental for separation and collection of photo-generated charge carriers. During the course of migration toward respective sites, some of the photogenerated electron-hole pairs were recombined either on the surface of NFs or in the electrolyte. This results in poor charge separation and collection, ultimately limiting the water oxidation performance. In contrast, the nanocoral morphology offers a thin hematite layer (thickness ~100−200 nm) consisting of voids surrounded by nanocoral edges that very effectively separate the photogenerated charge carriers. The close match of the hematite penetration depth with nano-coral thickness is advantageous for avoiding recombination losses. Moreover, the small voids of nanocoral structures in PRED-treated photoanode can easily adsorb the electrolyte on its surface and trap the photo-generated holes to effectively drive the water oxidation reaction.

Hence, PRED treatment has a beneficial role in improving interface properties, subsequently leading to stable and efficient water oxidation performance of $Fe_2O_3$/Fe photoanodes. Thus, the combined factors of stable interface of nanocoral structures, increased high-index [104] facet sites, and effective charge separation owing to decrease in charge transfer resistance are responsible for the water splitting performance enhancement in PRED-treated $Fe_2O_3$/Fe photoanodes. The water oxidation performance of such photoanodes could be further improved through controlled doping of different metals or formation of heterojunctions.

## Conclusions

In summary, efficient and stable $Fe_2O_3$/Fe photoanodes with nanostructured morphologies were successfully grown via thermal oxidation of Fe foil at 800 °C for 6 min. A mild electrochemical surface treatment of Fe foil in weak acidic electrolyte using a simple pulse reverse electrodeposition method was found to be beneficial for the growth of a stable nanostructured morphology. As studied from XPS depth profiling, PRED treatment is helpful in selective dissolution of the loosely bound $Fe_2O_3$ layer grown on Fe foil during air-exposure. Such treatment activates the surface of Fe foil for thermal oxidation, resulting in stable nano-coral morphology in contrast to the non-adherent and chemically unstable nano-flake morphology resulting from bare Fe foil without PRED treatment. PRED treatment also supports the formation of high-index [104] facet, which is a reportedly photo-catalytically-active site for heterogeneous water oxidation reactions. Compared to its counterpart, the PRED-treated photoanode showed photocurrent improvement with excellent chemical stability for extended duration in 1M NaOH under one sun illumination. The performance enhancement of PRED-treated nano-coral structures is attributed to the improved charge transfer kinetics and reduced recombination losses due to the stable interface of hematite and the exposure of high-index planes during water oxidation.

## Acknowledgements

This research was supported by BK Plus and the Basic Science Research Programs of the National Research Foundation of Korea (NRF, 2012R1A6A3A04038530), as well as the Korea Ministry of Environment (MOE) as Public Technology Program based on Environmental Policy. The authors greatly thank Mr. Yongmoon Lee of Yonsei University for his helpful discussion in analysis of diffraction profiles.

## Notes and references

1. K. Sivula, F. Le Formal and M. Grätzel, *ChemSusChem*, 2011, **4**, 432−449.
2. I. Cesar, K. Sivula, A. Kay, R. Zboril and M. Grätzel, *J. Phys. Chem. C*, 2009, **113**, 772−782.
3. I. Balberg and H. L. Pinch, *J. Magn. Magn. Mater.*, 1978, **7**, 12−15.
4. J. H. Kennedy and M. Anderman, *J. Electrochem. Soc.*, 1983, **130**, 848−852.
5. F. Le Formal, M. Graetzel and K. Sivula, *Adv. Funct. Mater.*, 2010, **20**, 1099−1107.
6. J. Brillet, M. Gratzel and K. Sivula, *Nano Lett.*, 2010, **10**, 4155−4160.
7. A. A. Tahir, K. U. Wijayantha, S. Saremi-Yarahmadi, M. Mazhar and V. McKee, *Chem. Mater.*, 2009, **21**, 3763−3772.
8. A. Kay, I. Cesar and M. Grätzel, *J. Am. Chem. Soc.*, 2006, **128**, 15714−15721.

9. R. Takagi, *J. Phys. Soc. Jpn.*, 1957, **12**, 1212−1218.
10. Y. Fu, J. Chen and H. Zhang, *Chem. Phys. Lett.*, 2001, **350**, 491−494.
11. S. Grigorescu, C.-Y. Lee, K. Lee, S. Albu, I. Paramasivam, I. Demetrescu and P. Schmuki, *Electrochem. Commun.*, 2012, **23**, 59−62.
12. X. Wen, S. Wang, Y. Ding, Z. L. Wang and S. Yang, *J. Phys. Chem. B*, 2005, **109**, 215-220.
13. L. Liao, Z. Zheng, B. Yan, J. Zhang, H. Gong, J. Li, C. Liu, Z. Shen and T. Yu, *J. Phys. Chem. C*, 2008, **112**, 10784−10788.
14. T. Vincent, M. Gross, H. Dotan and A. Rothschild, *Int. J. Hydrogen Energy*, 2012, **37**, 8102−8109.
15. L. Yuan, R. Cai, J. I. Jang, W. Zhu, C. Wang, Y. Wang and G. Zhou, *Nanoscale*, 2013, **5**, 7581−7588.
16. R. van de Krol, Y. Liang and J. Schoonman, *J. Mater. Chem.*, 2008, **18**, 2311−2320.
17. P. M. Rao and X. Zheng, *Nano Lett.*, 2009, **9**, 3001−3006.
18. J. Han, X. Zong, Z. Wang and C. Li, *Phys. Chem. Chem. Phys.*, 2014, **16**, 23544−23548.
19. P. S. Shinde, A. Annamalai, J. Y. Kim, S. H. Choi, J. S. Lee and J. S. Jang, *J. Phys. Chem. C*, 2015, **119**, 5281−5292.
20. P. S. Shinde, A. Annamalai, J. H. Kim, S. H. Choi, J. S. Lee and J. S. Jang, *Sol. Energy Mater. Sol. Cells*, 2015, **141**, 71−79.
21. J. F. Moulder, W. F. Stickle, P. E. Sobol and K. D. Bomben, *Handbook of X-ray Photoelectron Spectroscopy (Physical Electronics)*, Perkin-Elmer Corp, Eden Prairie, MN, 1995.
22. C. Aydın, M. S. Abd El-sadek, K. Zheng, I. S. Yahia and F. Yakuphanoglu, *Opt. Laser Technol.*, 2013, **48**, 447−452.
23. B. D. Chernomordik, H. B. Russell, U. Cvelbar, J. B. Jasinski, V. Kumar, T. Deutsch and M. K. Sunkara, *Nanotechnol.*, 2012, **23**, 194009−194017.
24. Y. Ling and Y. Li, *Part. Part. Syst. Charact.*, 2014, **31**, 1113−1121.
25. H. Schäfer, S. Sadaf, L. Walder, K. Kuepper, S. Dinklage, J. Wollschläger, L. Schneider, M. Steinhart, J. Hardege and D. Daum, *Energy Environ. Sci.*, 2015, DOI: 10.1039/c1035ee01601k.
26. H. Schäfer, S. M. Beladi-Mousavi, L. Walder, J. Wollschläger, O. Kuschel, S. Ichilmann, S. Sadaf, M. Steinhart, K. Küpper and L. Schneider, *ACS Catal.*, 2015, **5**, 2671−2680.
27. A. Larson and R. Von Dreele, *Report LAUR 86-748*.
28. W. Wu, R. Hao, F. Liu, X. Su and Y. Hou, *J. Mater. Chem. A*, 2013, **1**, 6888−6894.
29. B. Klahr, S. Gimenez, F. Fabregat-Santiago, T. Hamann and J. Bisquert, *J. Am. Chem. Soc.*, 2012, **134**, 4294−4302.
30. F. Schrettle, C. Kant, P. Lunkenheimer, F. Mayr, J. Deisenhofer and A. Loidl, *Eur. Phys. J. B*, 2012, **85**, 1−12.